Inorganic Chemistry

pubs.acs.org/IC

Featured Article

On TAML Catalyst Resting State Lifetimes: Kinetic, Mechanistic, and Theoretical Insight into Phosphate-Induced Demetalation of an Iron(III) Bis(sulfonamido)bis(amido)-TAML Catalyst

Hannah C. Frame, Longzhu Q. Shen, Alexander D. Ryabov,* and Terrence J. Collins*

Cite This: *Inorg. Chem.* 2023, 62, 639−647

Read Online

ACCESS | Metrics & More | Article Recommendations | Supporting Information

ABSTRACT: At ambient temperatures, neutral pH and ultralow concentrations (low nM), the bis(sulfonamido)bis(amido) oxidation catalyst $[Fe\{4\text{-}NO_2C_6H_3\text{-}1,2\text{-}(NCOCMe_2NSO_2)_2CHMe\}(OH_2)]^-$ (**1**) has been shown to catalyze the addition of an oxygen atom to microcystin-LR. This persistent bacterial toxin can contaminate surface waters and render drinking water sources unusable when nutrient concentrations favor cyanobacterial blooms. In mechanistic studies of this oxidation, while the pH was controlled with phosphate buffers, it became apparent that iron ejection from **1** becomes increasingly problematic with increasing [phosphate] (0.3−1.0 M); **1** is not noticeably impacted at low concentrations (0.01 M). At pH < 6.5 and [phosphate] ≥ 1.0 M, **1** decays quickly, losing iron from the macrocycle. Iron ejection is surprisingly mechanistically complex; the pseudo-first-order rate constant k_{obs} has an unusual dependence on the total phosphate concentration ($[P_t]$), $k_{obs} = k_1[P_t] + k_2[P_t]^2$, indicating two parallel pathways that are first and second order in [phosphate], respectively. The pH profiles in the 5.5−8.3 range for k_1 and k_2 are different: bell-shaped with a maximum of around pH 7 for k_1 and sigmoidal for k_2 with higher values at lower pH. Mechanistic proposals for the k_1 and k_2 pathways are detailed based on both the kinetic data and density functional theory analysis. The major difference between k_1 and k_2 is the involvement of different phosphate species, i.e., HPO_4^{2-} (k_1) and $H_2PO_4^-$ (k_2); HPO_4^{2-} is less acidic but more nucleophilic, which favors intramolecular rate-limiting Fe−N bond cleavage. Instead, $H_2PO_4^-$ acts intermolecularly, where the kinetics suggest that $[H_4P_2O_8]^{2-}$ drives degradation.

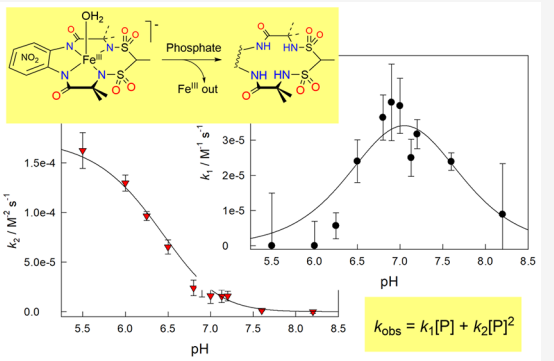

1. INTRODUCTION

TAML activators of peroxides[1] (Figure 1) are functional replicas of peroxidase enzymes that catalyze oxidative decontamination of persistent pollutants by hydrogen peroxide (H_2O_2) and organic peroxides in both laboratory and natural environments.[2−4] Recently, we have focused on bis(amido)-bis(sulfonamido) macrocyclic activators similar to **1** because of advantageous properties among the extended TAML family including higher catalytic activity with a pH-dependent rate optimum closest to the neutral region.[5,6] TAML **1** contains the >C*H*Me unit surrounded by two SO_2-sulfonamido-*N* functionalities. We refer to the unit as a catalyst "kill switch". The sulfonamido-*N* ligands of **1** deliver an increase in catalytic oxidative aggression compared to the carbonamido-*N* ligands of **2** that they replace and a pH-dependent change in dominating decomposition mechanisms for **1** versus **2**. The ideal TAML has a very reactive active state that lasts long enough to deliver an excellent catalytic performance but not so long that it persists when its targeted work is done. The lack of environmental persistence after use can be recognized as a safe and sustainable design element for oxidation catalysts.

For the prototype TAML activator, **2a**,[7] protons and general acids[8,9] at appropriate concentrations cause Fe^{III} ejection with liberation of the corresponding macrocyclic ligand. General acids such as mono- and dihydrogen phosphate are often components of buffer solutions in which the catalytic activity of TAMLs is explored.[10,11] On rare occasions, TAML catalysis is not observed in the absence of phosphate ions;[12] i.e., phosphate can be more than a pH controller and also serves as a promoter of catalysis. Thus, in building an extensive understanding of the catalytic cycle, it is important to understand the effects of phosphate on the latest generation of TAML activators, among which **1** is the optimal performer thus far. This need for deeper interrogation involves the resting state not only under operating conditions but also under nonoperating conditions to expand our appreciation of the

Received: November 1, 2022
Published: January 4, 2023

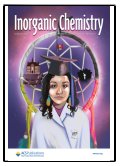

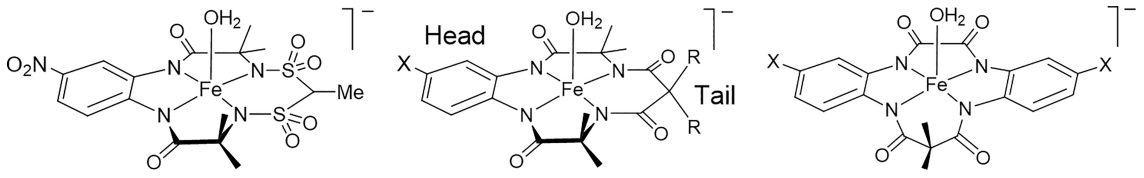

1 2 3

Figure 1. TAML activators used and mentioned in this work: X = H, R = Me (**a**); X = NO_2, R = F (**b**).

mechanistic intricacy and as a potential catalyst and process design information for improving catalytic performances. The existence of the "kill switch" (the acidic proton on the aforementioned −C*H*Me moiety, which following deprotonation can yield an oxidatively sensitive sulfur ylide) in **1** gives an additional reason for testing its stability in phosphate buffer solutions.

Therefore, we undertook a systematic kinetic and mechanistic investigation of the chemistry of **1** with phosphate ions. The results presented in this work show that phosphate causes slow pH-dependent Fe^{III} ejection from **1** in the pH range of 5.5−8.2. The ejection occurs in two parallel pathways: one first order and another second order in the total phosphate concentration. The pH profiles of these two pathways are remarkably different. Evidence is provided that phosphate binds to **1** and **2b**, although **2b** is much more resistant to demetalation. Mechanisms of iron ejection are put forward and discussed in detail using the kinetic information and the results of density functional theory (DFT) simulations.

2. EXPERIMENTAL SECTION

2.1. Methods: Chemicals, Instrumentation, and Procedures. TAML **1** was prepared as described elsewhere.[5] Further samples of **1** and samples of **2b** were provided by Sudoc, LLC. All other reagents were ACS grade and used without further purification.

UV−vis demetalation measurements were conducted in capped quartz cuvettes on a Cary 3500 spectrophotometer, engaging the air-cooled Peltier thermal control system as noted (typically 45 °C). Phosphate binding experiments were also conducted on a Cary 3500 spectrophotometer, with the cell-block temperature set to 15 °C. Aqueous stock solutions of **1** and **2b** were added to various concentrations of phosphate buffer (0.0−1.0 M) to reach final TAML concentrations of 3.5×10^{-5} M for each, and the resulting spectra were measured immediately.

The pH values of the buffers [prepared from mono- and dipotassium phosphate salts in high-performance liquid chromatography (HPLC) grade water and adjusted to the desired pH with a KOH solution as needed] were determined using a Fisherbrand Accumet AB15 pH meter calibrated to pH 4, 7, and 10. Phosphate buffers were reprepared weekly.

The pseudo-first-order rate constant k_{obs} for Fe^{III} ejection from **1** was calculated for faster reactions from the slopes of linear $\ln\{(A_0 - A_\infty)/(A_t - A_\infty)\}$ versus time t plots (A_0, A_∞, and A_t are the absorbances at time zero, infinity, and t, respectively). Kinetic data for slower processes were acquired by measuring the initial rates of demetalation at 358 nm using the values of extinction coefficients ε of 9660 and 9100 M^{-1} cm^{-1} for **1** and **2b**, respectively, plotting concentrations versus time in the linear portion of the graph.

2.1.1. Mass Spectral Analysis. A solution of 5.2×10^{-5} M **1** in 1.0 M pH 7 phosphate (3 mL) was prepared and left to demetalate at room temperature overnight (18 h), during which time all visible color faded. The mother liquor was washed with an equal volume of dichloromethane. The organic layer was separated and dried via rotary evaporation, before being redissolved and diluted to a theoretical concentration of 2.1×10^{-5} M (assuming quantitiative demetalation) in 50:50 methanol/water (H_2O) (0.1% formic acid) for mass spectral analysis. Analysis was conducted via direct injection with heated electrospray ionization in negative-ion mode (325 °C, 3.5 kV) on a Thermo Scientific Exactive Plus EMR Orbitrap mass spectrometer at the Carnegie Mellon University Center for Molecular Analysis.

2.2. DFT Calculations. *Gaussian 09*, revision D.01,[13] was employed to investigate separately the interactions between **1** and the two phosphate anions ($H_2PO_4^-$ and HPO_4^{2-}). The structure of **1** was built by modifying the X-ray data of its geometrical analogue without the nitro group.[5] The 3D structures of the phosphates ($H_2PO_4^-$ and HPO_4^{2-}) were created using the open-source chemistry toolbox *OpenBabel*.[14] Becke's three-parameter hybrid functional (B3)[15,16] with the Lee−Yang−Parr correlation (LYP)[17] and the 6-31+G(d) basis set were implemented in the computations. The SMD (solvation model based on density) continuum model was adopted to consider the solvent effect.[18] To explore the binding of two phosphate anions to **1**, two sets of computational experiments were carried out: (1) the axial water ligand replaced with $H_2PO_4^-$/HPO_4^{2-}; (2) competing binding between two axial ligands among every pair of HPO_4^{2-}, $H_2PO_4^-$, and H_2O. The final optimized molecular geometries were obtained after the computations converged to the default criteria.

3. RESULTS AND DISCUSSION

3.1. Phosphate-Induced Fe^{III} Ejection from 1. The solution of the TAML activator **1** does not show noticeable spectral changes at ambient temperature at pH 7.0 controlled by 0.01 M phosphate buffer for at least 48 h. The spectrum of **1** changes gradually with time at much higher phosphate concentrations (ca. 0.3−0.7 M), as shown in Figure 2. The maximal absorbance at 358 nm decreases, and two clear isosbestic points are observed at 282 and 315 nm, revealing the coexistence of two absorbing species in solution. These species

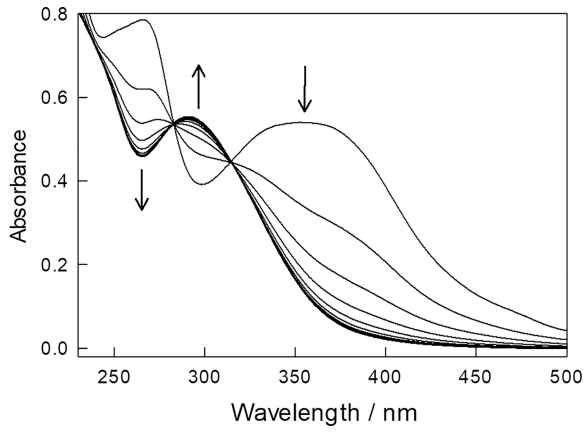

Figure 2. Spectral changes that accompany Fe^{III} ejection from **1** in the presence of phosphate. Conditions: [**1**] = 5.2×10^{-5} M, [phosphate] = 1.0 M, pH 7, and 45 °C. Spectra were recorded with 40 min intervals.

https://doi.org/10.1021/acs.inorgchem.2c03854
Inorg. Chem. 2023, 62, 639−647

are intact **1** and the free bis(sulfonamido)bis(amido) ligand **4** produced by the Fe^{III} ejection from **1** (eq 1).

$$[Fe\{4\text{-}NO_2C_6H_3\text{-}1,2\text{-}(NCOCMe_2NSO_2)_2CHMe\}(OH_2)]^- \ (\mathbf{1}) + 4H^+ \xrightarrow{\text{phosphate}} 4\text{-}NO_2C_6H_3\text{-}1,2\text{-}(NHCOCMe_2NHSO_2)_2CHMe \ (\mathbf{4}) + \text{“}Fe^{III}\text{”} \quad (1)$$

The isosbestic points such as those in Figure 2 look less perfect after prolonged time periods (over 1 day at 45 °C) tentatively due to a very slow ligand degradation.[19−23] No attempts were made here to study this process in detail.

The initial formation of free ligand **4** was confirmed by two methods. Reaction (1) was run for 18 h at room temperature, and **4** was extracted into dichloromethane. First, the UV−vis spectrum of the extracted material was measured and found to be identical with that of authentic **4** (Figure S1). Electrospray ionization mass spectrometry (ESI-MS) analysis of the solution revealed the presence of a single product, which was detected at m/z 476.09 in the negative-ion mode, as expected for **4** (Figures S2 and S3). No other products were observed.

3.2. Kinetic Data. The kinetics of demetalation (eq 1) is conveniently followed by UV−vis spectroscopy at 358 nm, where **1** has an absorption maximum at pH 7. The reaction is complete after ca. 24 h at [phosphate] > 0.5 M and 45 °C. The kinetic trace (Figure S4) is exponential, suggesting a first reaction order in **1**. The inset to Figure S4 shows linearization of the trace using the $\ln\{(A_0 - A_\infty)/(A_t - A_\infty)\}$ versus time t plot (A_t is the absorbance at time t).[24] The pseudo-first-order rate constants k_{obs} for decomposition of **1** are the slopes of linear plots. The linearity is commonly observed for more than five half-lives, proving a solid case for first order in **1**. This allowed us to measure the initial rates (v) of reaction (1), which are much lower at lower phosphate concentrations, and calculate k_{obs} as a ratio of $v/[\mathbf{1}]$ because $v = k_{obs}[\mathbf{1}]$. It was confirmed that identical values of k_{obs} are obtained from the linearization of all kinetic traces and using the $v/[\mathbf{1}]$ routine.

The dependence of k_{obs} for reaction (1) on the total phosphate concentration ($[P_t]$), as presented in Figure 3, is not linear. There is a positive deviation from the straight line, with the effect becoming more pronounced at lower pH. The nonlinear dependence suggests that reaction (1) occurs via two parallel pathways, viz., one first order and another second order in $[P_t]$. Therefore, the data in Figure 3 were fitted to eq 2, and the best-fit values of k_1 and k_2 obtained in the pH range 5.5−8.3 are collected in Table 1.

$$k_{obs} = k_1[P_t] + k_2[P_t]^2 \quad (2)$$

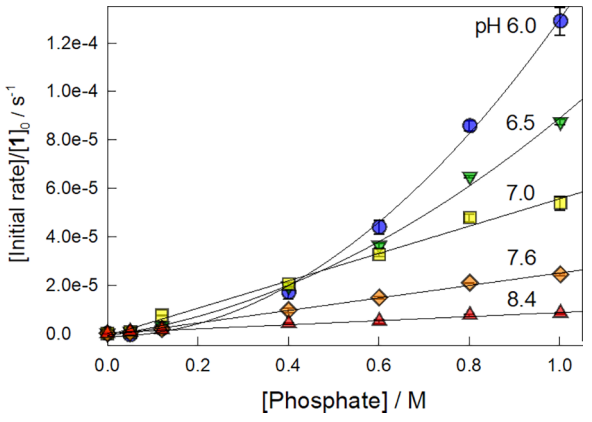

Figure 3. Influence of the pH on representative dependences of k_{obs} for the degradation of **1** (eq 1) on the total phosphate concentration ($[P_t]$) consistent with eq 2. Data were obtained at 45 °C. The solid lines are calculated curves using the best-fit values of k_1 and k_2 presented in Table 1 (see the text for details).

Table 1. Rate Constants k_1 and k_2 (45 °C) for the Demetalation of 1 Calculated from the Data such as in Figure 3

entry	pH	$10^5 \times k_1/M^{-1}\ s^{-1}$	$10^5 \times k_2/M^{-2}\ s^{-1}$
1	4.75	n.o.[a]	30 ± 4
2	5.5	n.o.	16 ± 2
3	6.0	n.o.	13 ± 8
4	6.25	0.6 ± 0.4	9.6 ± 0.4
5	6.5	2.4 ± 0.6	6.5 ± 0.7
6	6.8	3.6 ± 0.6	2.4 ± 0.8
7	6.9	4.1 ± 0.1	3 ± 1
8	7.0	4.0 ± 0.8	1.6 ± 0.8
9	7.13	2.5 ± 0.5	1.6 ± 0.6
10	7.2	3.2 ± 0.4	1.6 ± 0.5
11	7.6	2.4 ± 0.2	1.2 ± 0.3
12	8.2	n.o.	n.o.

[a]Negligible or not observed.

The phosphate concentration was varied in a broad range, and therefore k_{obs} could be a function of the ionic strength. To rule out the ionic strength effect, the reaction rates were measured in the presence of added KPF_6. The data presented in Figure S5 show that the effect of neutral salts is negligible compared to that of phosphate.

The contributions of the first- and second-order pathways vary with the pH. The second-order k_2 pathway is insignificant at pH ≥ 7 and practically unobservable at pH > 12. The first-order k_1 pathway starts to show up at pH > 6 and disappears at pH > 11. Different reaction orders in phosphate as the pH changes indicate that the phosphate species involved in the first- and second-order reaction pathways most likely have different protonation states. Mechanistic consequences of this finding are discussed below.

It is of interest to compare **1**, which is a bis(sulfonamido)-bis(amido) species, with **2b**, a tetraamido species, the TAML activator previously considered by us as having the best balance of technical performance parameters, rate constants of activation, oxidation of a benchmark substrate, and TAML degradation.[25] Catalyst **2b** is much more resilient than **1** to the always slow phosphate-induced demetalation described herein, and therefore just the initial rates of the iron ejection for **2b** could be measured. The comparison of the initial rates of demetalation of **1** and **2b** in Figure 4 shows that, at phosphate concentrations above 0.2 M, the iron ejection from **1** occurs much faster than that from **2b**, with the rate ratio being a factor of 54 at 1.0 M [phosphate] (pH 7). Such a rate variation indicates that **1** is more sensitive to general acids such as phosphate species compared to **2b**. There is no parallel difference with the $Fe^{III/IV}$ reduction potentials of **1** and **2b**, which are very close (1.19 and 1.16 V[26] vs saturated calomel electrode, respectively, in acetonitrile), where the $Fe^{III/IV}$ couple probably involves the bis(acetonitrile) complex. Considering that differing reduction potentials likely reflect the electron density at each TAML, the rather different

https://doi.org/10.1021/acs.inorgchem.2c03854
Inorg. Chem. 2023, 62, 639−647

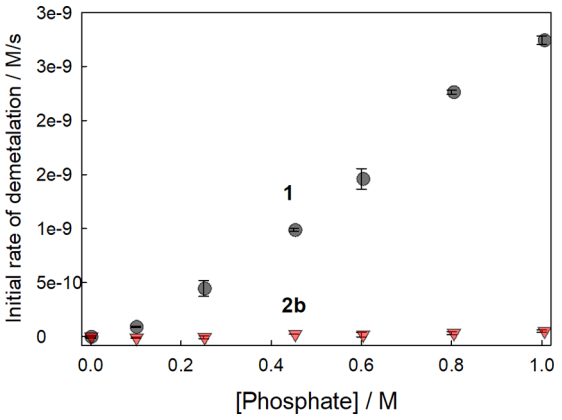

Figure 4. Comparison of the initial rates of phosphate-induced demetalation of **1** and **2b**. Conditions: both [**1**] and [**2b**] = 5.2×10^{-5} M, pH 7.0, 45 °C.

demetalation rates of **1** and **2b** are a signal that multiple interactions between the phosphate acid anions and the TAMLs are in play.

A comparison of the structures of **1** and **2b** (Figure 1) through the prism of the data in Figure 4 suggests which Fe−N bond of **1**, i.e., in the head or in the tail, is a primary target of phosphate species. The head parts, including two carbonamido nitrogen atoms, of **1** and **2b** are identical. The tail parts are different. Because the reactivity of **1** and **2b** with phosphate anions is diverse, it follows as reasonable that a sulfonamido nitrogen atom of **1** first accepts a proton, leading to cleavage of an Fe−N bond. This step is likely rate-limiting because cleavage of just one Fe−N bond should eliminate the TAML-constrained planarity, allowing TAML distortions to enhance the rates of cleavage of the remaining Fe−N bonds.[7]

3.3. pH Profiles for k_1 and k_2 and Their Interpretations. The rate constants k_1 and k_2 are both pH-dependent, but the profiles vary distinctively (Figure 5). The profile for k_1 is bell-shaped in the pH range of 5.5−8.3 with a maximum of around pH 7, but for k_2, it is sigmoidal and the rate constants increase with decreasing pH. Such sigmoidal dependencies were previously observed for **2a**[8] and **3**,[9] but in those cases, the demetalation reactions were first-order in phosphate and not second-order, as with **1**. Larger experimental errors in Figure 5A are due to the fact that the second-order pathway in phosphate is dominant. The contribution from the first-order pathway is much lower. Thus, the kinetic information regarding the k_1 pathway is collected when the "background" rates originating from the k_2 pathway are much higher. This automatically causes lower accuracy in determining the k_1 values (particularly at lower pH in this range).

3.3.1. k_1 Pathway. A bell-shaped pH dependence for k_1 with a maximum of around 7 (Figure 5A) can be mechanistically rationalized by assuming that the monohydrogen phosphate (HPO_4^{2-}) causes the degradation of **1**, whereas dihydrogen phosphate ($H_2PO_4^-$) is significantly less reactive. This postulate accounts for a sharp decrease in k_1 to zero at pH < 6.5. The decrease in k_1 at pH > 7.5 is presumably associated with the deprotonation of an axial water of **1** to form the hydroxo species.

The hydroxo ligand is a poor leaving group; it is more strongly coordinated to Fe^{III} than the water ligand, which, if the Fe^{III} is five-coordinate at all times, will reduce the ability of HPO_4^{2-} to enter the coordination sphere or, if the Fe^{III} is six-coordinate, reduces the water binding constant by virtue of its higher trans influence. The exact steps of the suggested mechanism are represented in Scheme 1A, assuming that the five-coordinate structure is favored. Equation 3 is the corresponding rate law, which is consistent with the pH dependence of k_1 in Figure 5A.

$$k_1 = \frac{kK_{a2}^{P}[H^+]}{[H^+]^2 + (K_{a2}^{P} + K_{a1})[H^+] + K_{a2}^{P}K_{a1}} \quad (3)$$

Because $K_{a2}^{P} \gg K_{a1}$, eq 3 can be rewritten as eq 4.

$$k_1 = \frac{kK_{a2}^{P}[H^+]}{[H^+]^2 + K_{a2}^{P}[H^+] + K_{a2}^{P}K_{a1}} \quad (4)$$

Equation 4 accounts for the pH dependence of k_1 in Figure 5A. Fitting the experimental data to eq 4, assuming pK^{P}_{a2} = 6.75 and pK_{a1} = 7.35 at 45 °C (8.8 at 25 °C),[5] allows an estimation of the value of $k = (6.8 \pm 0.5) \times 10^{-5}$ M^{-1} s^{-1} and the calculation of a theoretical curve, which shows a resemblance with the experimental values of k_1 in Figure 5A.

The most challenging and curious feature of the mechanism in Scheme 1A is that HPO_4^{2-} and not the more acidic $H_2PO_4^-$ is the reactive species in the k_1 pathway. The evidence for HPO_4^{2-} as the key actor in Figure 5A is straightforward because otherwise the bell-shaped dependence would not be observed. Our hypothesis is that both the acidity and

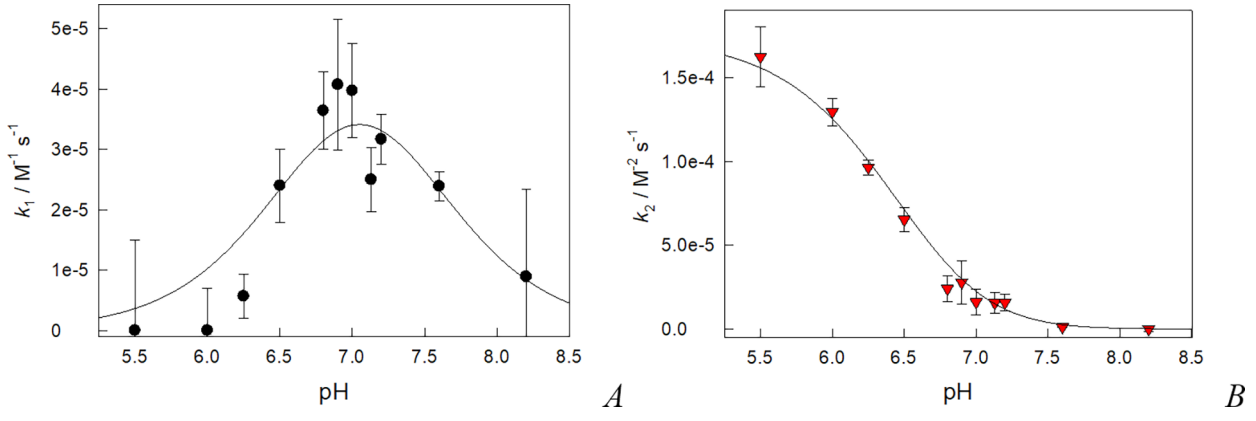

Figure 5. pH dependencies of k_1 (A) and k_2 (B) at 45 °C. The solid lines were calculated using the best-fit values of k_1 (A) and $k_{11}K_3$ (B) assuming pK^{P}_{a2} = 6.75 (A and B) and pK_{a1} = 7.35 (A). See the text for details.

https://doi.org/10.1021/acs.inorgchem.2c03854
Inorg. Chem. 2023, 62, 639−647

Scheme 1A. Plausible Stoichiometric Mechanism of the k_1 Pathway in Phosphate Demetalation Formally Consistent with Its pH Profile (Figure 5A)

$$H_2PO_4^- \rightleftarrows HPO_4^{2-} + H^+ \qquad (K^P_{a2})$$

$$[FeL(OH_2)]^- \rightleftarrows [FeL(OH)]^{2-} + H^+ \qquad (K_{a1})$$

$$HPO_4^{2-} + [FeL(OH_2)]^- \rightarrow \text{Degradation products} \qquad (k)$$

Scheme 1B. Final Steps of the "Intramolecular" Variant of the Mechanism Presented in Scheme 1A

$$HPO_4^{2-} + [FeL(OH_2)]^- \rightleftarrows [FeL(HPO_4)]^{3-} \qquad (K')$$

$$[FeL(HPO_4)]^{3-} \rightarrow \text{Degradation products} \qquad (k')$$

Scheme 2. Plausible Stoichiometric Mechanism of the k_2 Pathway Formally Consistent with Its pH Profile (Figure 5B)

$$H_2PO_4^- \rightleftarrows HPO_4^{2-} + H^+ \qquad (K^P_{a2})$$

$$[FeL(OH_2)]^- + H_2PO_4^- \rightleftarrows [FeL(H_2PO_4)]^{2-} \qquad (K_3)$$

$$[FeL(H_2PO_4)]^{2-} + H_2PO_4^- \rightarrow \text{Degradation products} \qquad (k_{11})$$

Scheme 3. Alternative Stoichiometric Mechanism of the k_2 Pathway Formally Consistent with Its pH Profile in Figure 5B

$$H_2PO_4^- \rightleftarrows HPO_4^{2-} + H^+ \qquad (K^P_{a2})$$

$$[FeL(OH_2)]^- + 2\,H_2PO_4^- \rightleftarrows [FeL(H_2PO_4)_2]^{3-} \qquad (K_3)$$

$$[FeL(H_2PO_4)_2]^{3-} \rightarrow \text{Degradation products} \qquad (k_{11})$$

nucleophilicity of the phosphate species play significant roles. $H_2PO_4^-$ is more acidic although less nucleophilic than HPO_4^{2-}. HPO_4^{2-} should be a better incoming ligand into the coordination sphere of Fe^{III}. If the anation by HPO_4^{2-} is essential, Fe−N bond cleavage should be intramolecular and the last step in Scheme 1A should be detailed as shown in Scheme 1B.

For this variant, $k = k'K'$. This mechanistic version in Scheme 1B makes it more obvious why deprotonation of the aqua ligand freezes out the k_1 pathway. In the all-five-coordination pathway, coordination of HPO_4^{2-} becomes less likely due to the formation of a poor leaving hydroxo ligand such that the intramolecular step of Scheme 1B cannot occur. This hypothesis is supported by the results of DFT analysis described below.

3.3.2. k_2 Pathway. The pH profile of k_2, which is second-order in phosphate, with the inflection point around 6.5, matches the profile previously reported for the phosphate-induced demetalation of **2a**, although that process obeyed first-order kinetics in total phosphate.[8] Such a changeover of the reaction order is intriguing. An obvious starter mechanistic hypothesis is that a single dihydrogen phosphate unit is unable to demetalate/destroy **1** such that a second $H_2PO_4^-$ unit is required. A variant of the reaction mechanism is presented in Scheme 2. It includes first reversible phosphate binding to Fe^{III} (K_3), followed by a rate-limiting intermolecular interaction of the iron phosphate complex and dihydrogen phosphate (k_{11}).

In the most general case, Scheme 2 leads to the following expression for the rate of the second-order pathway in phosphate:

$$v = \frac{k_{11}K_3[M_t][P_t]^2[H^+]^2}{(K^P_{a2} + [H^+])([P_t][H^+]K_3 + K^P_{a2} + [H^+])} \qquad (5)$$

Here $[M_t]$ and $[P_t]$ are the total concentrations of **1** and phosphate, respectively. The equation was obtained assuming that $[M_t] \ll [P_t]$ and using the mass balance equation $[M_t] = [M] + [MP]$, where M and MP are free and complexed forms of **1**. Second-order kinetics in the total phosphate concentration will be observed when $[P_t][H^+]K_3 \ll (K^P_{a2} + [H^+])$. Then eq 5 becomes

$$v = \frac{k_{11}[M_t][P_t]^2K_3[H^+]^2}{(K^P_{a2} + [H^+])^2}$$

which can be rewritten as eq 6, where k_2 is formally a trimolecular rate constant from eq 2.

$$k_2 = \frac{k_{11}K_3[H^+]^2}{(K^P_{a2} + [H^+])^2} \qquad (6)$$

Equation 5 accounts for the square-sigmoidal pH dependence of k_2 in Figure 5B. Fitting the experimental data to eq 6, assuming that $pK^P_{a2} = 6.75$ as above, allows for estimation of the value of the product $k_{11}K_3$ of $(1.74 \pm 0.04) \times 10^{-4}\ M^{-2}\ s^{-1}$ and calculation of a theoretical curve that agrees with the experimental values of k_2 in Figure 5B.

The mechanism of the k_2 pathway in Scheme 2 assumes that dihydrogen phosphate attacks the Fe^{III} species from the bulk, i.e., without the formation of a bis(phosphate) complex, which could further be involved in intramolecular demetalation (Scheme 3). The mechanisms in Schemes 2 and 3 imply at

https://doi.org/10.1021/acs.inorgchem.2c03854
Inorg. Chem. 2023, 62, 639−647

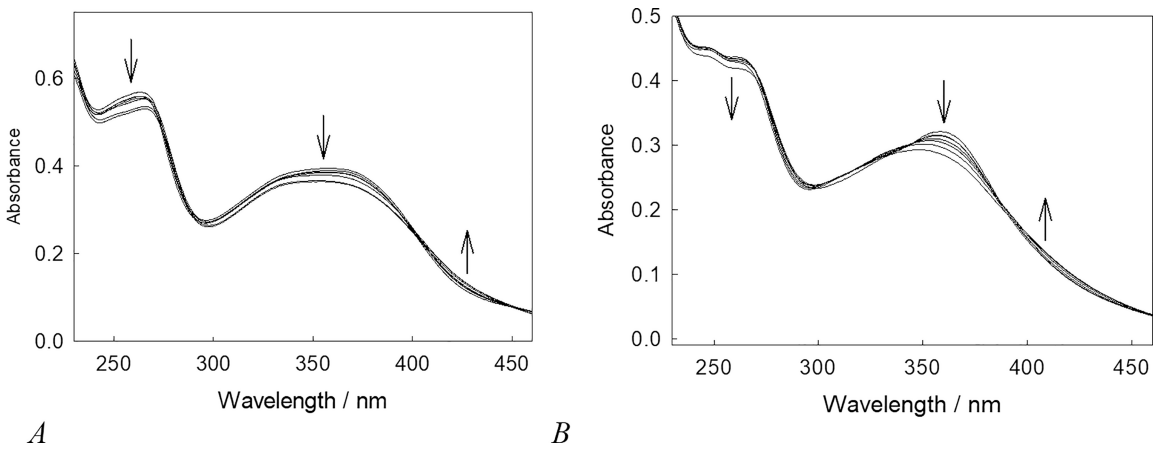

Figure 6. Spectral changes of **1** (A) and **2b** (B) recorded in the presence of increasing concentrations of phosphate in the range from 0 to 1.0 M. Conditions: both [**1**] and [**2b**] = 5.2×10^{-5} M, pH 7, and 15 °C.

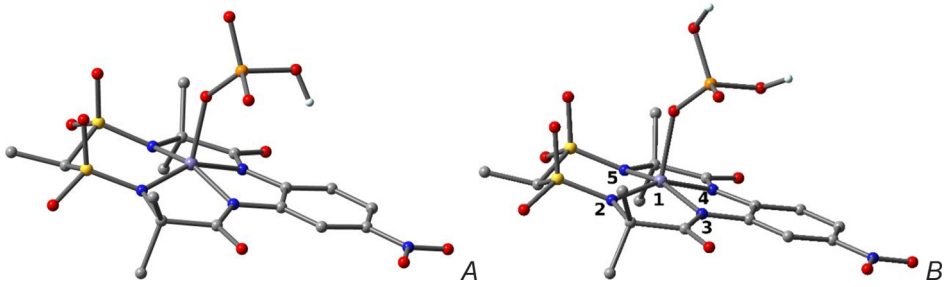

Figure 7. DFT-calculated structures of $[FeL(HPO_4^{2-})]^{3-}$ (A) and $[FeL(H_2PO_4^{-})]^{2-}$ (B). Hydrogen atoms other than those associated with phosphate residues are not shown for clarity.

high phosphate concentrations (which are impossible to achieve in practice) that the reaction order in phosphate should be different, i.e., 1 and 0, respectively. The former result comes from eq 5 because if $[P_t] \rightarrow \infty$,

$$v = \frac{k_{11}[M_t][P_t][H^+]}{K_{a2}^P + [H^+]}$$

Qualitatively, if the mechanism in Scheme 3 is operative and $[P_t] \rightarrow \infty$, all Fe^{III} should hypothetically be converted in the reactive MP_2 form and therefore the reaction rate should not depend on the phosphate concentration. Kinetic analysis of the scheme proposed agrees with the conclusion because in this case the general equation is

$$v = \frac{k_{11}K_3[M_t][P_t]^2[H^+]^2}{(K_{a2}^P + [H^+])^2 + K_3[H^+](K_{a2}^P + [H^+])[P_t]^2} \quad (7)$$

If $[P_t] \rightarrow \infty$,

$$v = \frac{k_{11}[M_t][H^+]}{K_{a2}^P + [H^+]}$$

Thus, the reaction rate shows no dependence on the phosphate concentration. At the same time, at low $[P_t]$, eq 7 becomes kinetically indistinguishable from eq 6, with the only difference being the formal units for k_{11} and K_3 used in Schemes 2 and 3 (M^{-1} s^{-1} and M^{-1} versus s^{-1} and M^{-2}, respectively).

3.4. Spectral Evidence for Phosphite Binding to 1 and 2b. The mechanisms in Schemes 1A–3 assume binding of phosphate to the resting state of **1**. Previously, no evidence was found by UV–vis spectroscopy for phosphate binding to **2a**.[8] With complexes **1** and **2b**, the Lewis acidity of which significantly exceeds that of **2a**, such evidence was acquired. The temperature was decreased to 15 °C to ensure better phosphate binding. The UV–vis spectra of both **1** and **2b** change as the phosphate concentration increases up to 1 M (Figure 6A,B). The absorbance of **1** decreases slightly, the maximum moves from 358 to 354 nm, and two isosbestic points are seen at 402 and 452 nm. This is consistent with the presence of just two absorbing species in solution. Spectral changes are more pronounced in the case of **2b**. There is a profound shift in the absorbance maximum (from 358 to 346 nm) with isosbestic points at 390, 343, and 306 nm. The spectral changes in both cases are most likely due to the binding of one, not two, phosphate units to the Fe^{III} of TAMLs. The formation of diphosphate species is rather improbable. If it were indeed forming, the concentration of the monophosphate species should be negligible and non-contributing to the overall spectral changes.

3.5. Probing the Two Parallel Pathways by DFT. *3.5.1. Phosphate Binding to Fe^{III} of 1: $H_2PO_4^-$ versus HPO_4^{2-}.* DFT investigation indicates different abilities of $H_2PO_4^-$ versus HPO_4^{2-} to coordinate to Fe^{III} in **1**. The former is a weaker ligand compared to the latter. The competitive binding between HPO_4^{2-} and H_2O to Fe^{III} of $[FeL(H_2O)]^-$ ended up with an effective pentadentate species when H_2O drifted out of the coordination sphere. The optimized structure of $[FeL(HPO_4^{2-})]^{3-}$ produced as a result of water replacement is shown in Figure 7A. A similar structure could be generated by ligating the vacant site of $[FeL]^-$ with HPO_4^{2-}. Both approaches led to similar results. The overlay of the optimized

https://doi.org/10.1021/acs.inorgchem.2c03854
Inorg. Chem. 2023, 62, 639–647

Table 2. Selected Bond Distances (Å) and Bond Angles (deg) Calculated for 1 and Its Complexes with Water and Mono- and Dihydrogen Phosphate[a]

	Fe−N2	Fe−N3	N2−Fe−N5	N3−Fe−N4	N2−Fe−N3
$[FeL(OH_2)]^-$	1.94	1.89	106.5	83.6	83.6
$[FeL(H_2PO_4^-)]^{2-}$	1.96	1.90	104.3	82.9	82.6
$[FeL(HPO_4^{2-})]^{3-}$	1.97	1.91	103.1	82.5	82.2

[a]The nitrogen numbering is indicated in Figure 7B.

Scheme 4. DFT-Inspired Variant of the Mechanism of the k_2 Pathway

$$H_2PO_4^- \rightleftarrows HPO_4^{2-} + H^+ \qquad (K^P_{a2})$$

$$2\ H_2PO_4^- \rightleftarrows [H_4P_2O_8]^{2-} \qquad (K_d)$$

$$[FeL(OH_2)]^- + [H_4P_2O_8]^{2-} \rightarrow \text{Products} \qquad (k'')$$

structures from the two theoretical experiments is presented in Figure S6.

A higher affinity of HPO_4^{2-} toward Fe^{III} of **1** was additionally confirmed in a set of "competitive" experiments. The starting material was the hypothetical high-energy pseudooctahedral complex $[FeL(HPO_4^{2-})(H_2PO_4^-)]^{4-}$. Axial sites were populated by HPO_4^{2-} and $H_2PO_4^-$, and one of them had to dissociate via eq 8 or 9 to form a corresponding five-coordinate species, as is shown in eqs 8 and 9.

$$[FeL(HPO_4^{2-})(H_2PO_4^-)]^{4-} \rightleftarrows [FeL(H_2PO_4^-)]^{2-} + HPO_4^{2-} \qquad (8)$$

$$[FeL(HPO_4^{2-})(H_2PO_4^-)]^{4-} \rightleftarrows [FeL(HPO_4^{2-})]^{3-} + H_2PO_4^- \qquad (9)$$

Optimization clearly shows that HPO_4^{2-} holds the thermodynamic preference. Equation 9 describes the dissociation of $H_2PO_4^-$. The "kill switch" unit >CHMe makes two positional isomers of $[FeL(HPO_4^{2-})(H_2PO_4^-)]^{4-}$ with HPO_4^{2-} syn or anti with respect to the methyl group of the switch. It was found that the initial position of HPO_4^{2-} is not important and the resultant complex contains bound HPO_4^{2-}. Conversely, $H_2PO_4^-$ is moving away from the first coordination sphere, leaving the option for a weak interaction within the second coordination sphere. Such a scenario has been considered in detail in our previous work.[12] In our opinion, this experiment presents even stronger evidence for a higher affinity of HPO_4^{2-} versus $H_2PO_4^-$ toward Fe^{III} of TAML **1**.

The structure of $([FeL(H_2PO_4^-)]^{2-}$ in Figure 7B was obtained by substitution of the aqua ligand. In comparison to the binding of HPO_4^{2-}, the case with $H_2PO_4^-$ caused less distortion of the coordination sphere of Fe^{III}. The structural alterations of **1** after ligation of $H_2PO_4^-$ and HPO_4^{2-} were significant. They provide a clue for understanding the different susceptibilities of $FeL(HPO_4^{2-})]^{3-}$ and $[FeL(H_2PO_4^-)]^{2-}$ to protonolysis. A distortion of the TAML ligand plane enhances the rates of protonolysis of Fe^{III} TAMLs.[7] The essential bond distances and bond angles calculated for $[FeL(OH_2)]^-$, $[FeL(HPO_4^{2-})]^{3-}$, and $[FeL(H_2PO_4^-)]^{2-}$ are compared in Table 2.

The HPO_4^{2-} pulls Fe^{III} more out of the plane made up by its four surrounding macrocyclic nitrogen atoms in comparison to its $H_2PO_4^{2-}$ analogue. The Fe−N bond distances become more elongated, which facilitates rate-limiting cleavage of the first Fe−N bond. These theoretical conclusions are fully consistent with the results of the kinetic studies, pointing to the importance of the stronger Lewis basicity of HPO_4^{2-} compared to that of $H_2PO_4^-$.

3.5.2. DFT Suggesting Alternative Rationalization of the k_2 Pathway. Competing binding of $H_2PO_4^-$ to the aqua species **1** led to computational instability. This suggests that the $[FeL(H_2PO_4^-)]^{2-}$ species may not readily form in large quantities in water and leads one to consider other pathways that establish second order in phosphate in the k_2 process without the intermediacy of iron phosphate complexes. Second order may arise from the dimerization of dihydrogen phosphate, as in Scheme 4, to form a species that is more electrophilic and therefore more reactive than the monomer species. The dimer species then reacts with **1** intermolecularly in the rate-limiting step.

There is significant general experimental,[27−29] kinetic,[30] and theoretical[31] evidence for the dimerization of dihydrogen phosphate. Interestingly, the dimerization is a feature of dihydrogen phosphate only (monohydrogen phosphate does not form dimers). Trimerization does not occur. The dimerization stability constant K_d is around 2−3 M^{-1}.[30] The dimer is thus not a dominating species; the dimerization equilibrium is shifted to the left and therefore

$$k_2 = \frac{k'' K_d [H^+]^2}{(K^P_{a2} + [H^+])^2} \qquad (10)$$

Equation 10 is kinetically indistinguishable from eq 6. Therefore, this theoretical insight has led us to consider Scheme 4 to account for a second order in the phosphate concentration (k_2).

4. CONCLUSION

In this contribution, we have added another set of novel processes to the panoply of equilibria and reactions that come into play when TAML catalysts in water are mixed with other chemicals. The process discovered is a slow TAML catalyst decomposition under nonoperating conditions, and it provides a process design signal that strong buffer solutions and **1** are not compatible for anything other than very rapid catalytic use. Perhaps the most challenging aspect of the present mechanistic investigation was the observation of two parallel pathways in the phosphate-induced demetalation of **1**, where we have been able to observe the pathways in action and discover the

https://doi.org/10.1021/acs.inorgchem.2c03854
Inorg. Chem. 2023, 62, 639−647

intrinsic reasons for their existence. There are two reactive phosphate species in the pH range investigated, viz., $H_2PO_4^-$ and HPO_4^{2-}. The former is more acidic, and the latter is more nucleophilic. This acidity/nucleophilicity balance plays a delicate role here. The poorer nucleophile ($H_2PO_4^-$) is unable to bind to Fe^{III} of **1** and has to deliver the proton at the Fe−N bond intermolecularly, presumably in the form of dimer $H_4P_2O_8^{2-}$, which is needed in order to increase the acidity of the phosphate species. The stronger nucleophile (HPO_4^{2-}) is capable of replacing the aqua ligand and binding to Fe^{III}. Its lower acidity compared to $H_2PO_4^-$ is compensated for by the intermolecular to intramolecular mechanistic changeover, and this is how the nucleophilic properties of a ligand assist in performing the rate-limiting protonolysis of the first Fe−N bond of TAML activator **1**.

■ ASSOCIATED CONTENT

Supporting Information

The Supporting Information is available free of charge at https://pubs.acs.org/doi/10.1021/acs.inorgchem.2c03854.

UV−visible and ESI-MS spectra of the product of demetalation of **1**, linearization of the exponential demetalation kinetics, effect of KPF_6 on the demetalation speed, and a comparison of the DFT structures of **1** with aqua and phosphate ligands (PDF)

■ AUTHOR INFORMATION

Corresponding Authors

Alexander D. Ryabov − *Department of Chemistry, Carnegie Mellon University, Pittsburgh, Pennsylvania 15213, United States;* orcid.org/0000-0002-5255-1395; Email: ryabov@andrew.cmu.edu

Terrence J. Collins − *Department of Chemistry, Carnegie Mellon University, Pittsburgh, Pennsylvania 15213, United States;* orcid.org/0000-0003-2611-9184; Email: tc1u@andrew.cmu.edu

Authors

Hannah C. Frame − *Department of Chemistry, Carnegie Mellon University, Pittsburgh, Pennsylvania 15213, United States;* orcid.org/0000-0002-6803-8035

Longzhu Q. Shen − *Faculty of Geoinformation Science and Earth Observation, University of Twente, Enschede 7514AE, The Netherlands;* orcid.org/0000-0001-5629-3007

Complete contact information is available at: https://pubs.acs.org/10.1021/acs.inorgchem.2c03854

Notes

The authors declare no competing financial interest.

■ ACKNOWLEDGMENTS

T.J.C. thanks the Heinz Family Foundation, the Axios Fund, and Korein-Tillery for support. The instrumentation used at the Center for Molecular Analysis at Carnegie Mellon University is funded by NSF Grant DBI-9729351.

■ REFERENCES

(1) Collins, T. J. TAML oxidant activators: a new approach to the activation of hydrogen peroxide for environmentally significant problems. *Acc. Chem. Res.* **2002**, *35* (9), 782−790.

(2) Collins, T. J.; Khetan, S. K.; Ryabov, A. D.Chemistry and applications of iron-TAML catalysts in green oxidation processes based on hydrogen peroxide. In *Handbook of Green Chemistry*; Anastas, P. T., Crabtree, R. H., Eds.; Wiley-VCH Verlag GmbH & KgaA: Weinheim, Germany, 2010; pp 39−77.

(3) Ryabov, A. D.; Collins, T. J. Mechanistic considerations on the reactivity of green Fe^{III}-TAML activators of peroxides. *Adv. Inorg. Chem.* **2009**, *61*, 471−521.

(4) Collins, T. J.; Ryabov, A. D. Targeting of high-valent iron-TAML activators at hydrocarbons and beyond. *Chem. Rev.* **2017**, *117* (13), 9140−9162.

(5) Warner, G. R.; Somasundar, Y.; Jansen, K. C.; Kaaret, E. Z.; Weng, C.; Burton, A. E.; Mills, M. R.; Shen, L. Q.; Ryabov, A. D.; Pros, G.; Pintauer, T.; Biswas, S.; Hendrich, M. P.; Taylor, J. A.; Vom Saal, F. S.; Collins, T. J. Bioinspired, multidisciplinary, iterative catalyst design creates the highest performance peroxidase mimics and the field of sustainable ultradilute oxidation catalysis. *ACS Catal.* **2019**, *9* (8), 7023−7037.

(6) Warner, G. R.; Somasundar, Y.; Weng, C.; Akin, M. H.; Ryabov, A. D.; Collins, T. J. Zero-order catalysis in the TAML-Catalyzed Oxidations of Imidacloprid and 3-Methyl-4-nitrophenol by H_2O_2 or Should a Catalyst Always Increase a Reaction Rate? *Chem. Eur. J.* **2020**, *26* (34), 7631−7637.

(7) Ghosh, A.; Ryabov, A. D.; Mayer, S. M.; Horner, D. C.; Prasuhn, D. E., Jr; Sen Gupta, S.; Vuocolo, L.; Culver, C.; Hendrich, M. P.; Rickard, C. E. F.; Norman, R. E.; Horwitz, C. P.; Collins, T. J. Understanding the mechanism of H+-induced demetalation as a design strategy for robust iron(III) peroxide-activating catalysts. *J. Am. Chem. Soc.* **2003**, *125* (41), 12378−12379.

(8) Polshin, V.; Popescu, D.-L.; Fischer, A.; Chanda, A.; Horner, D. C.; Beach, E. S.; Henry, J.; Qian, Y.-L.; Horwitz, C. P.; Lente, G.; Fabian, I.; Münck, E.; Bominaar, E. L.; Ryabov, A. D.; Collins, T. J. Attaining control by design over the hydrolytic stability of Fe-TAML oxidation catalysts. *J. Am. Chem. Soc.* **2008**, *130* (13), 4497−4506.

(9) Ellis, W. C.; Tran, C. T.; Roy, R.; Rusten, M.; Fischer, A.; Ryabov, A. D.; Blumberg, B.; Collins, T. J. Designing green oxidation catalysts for purifying environmental waters. *J. Am. Chem. Soc.* **2010**, *132* (28), 9774−9781.

(10) Chahbane, N.; Popescu, D.-L.; Mitchell, D. A.; Chanda, A.; Lenoir, D.; Ryabov, A. D.; Schramm, K.-W.; Collins, T. J. FeIII-TAML-catalyzed green oxidative degradation of the azo dye Orange II by H2O2 and organic peroxides: products, toxicity, kinetics, and mechanisms. *Green Chem.* **2007**, *9* (1), 49−57.

(11) Ghosh, A.; Mitchell, D. A.; Chanda, A.; Ryabov, A. D.; Popescu, D. L.; Upham, E.; Collins, G. J.; Collins, T. J. Catalase-peroxidase activity of iron(III)-TAML activators of hydrogen peroxide. *J. Am. Chem. Soc.* **2008**, *130* (45), 15116−15126.

(12) Kundu, S.; Shen, L. Q.; Somasundar, Y.; Annavajhala, M.; Ryabov, A. D.; Collins, T. J. TAML- and Buffer-Catalyzed Oxidation of Picric Acid by H2O2: Products, Kinetics, DFT, and the Mechanism of Dual Catalysis. *Inorg. Chem.* **2020**, *59* (18), 13223−13232.

(13) Frisch, M. J.; Trucks, G. W.; Schlegel, H. B.; Scuseria, G. E.; Robb, M. A.; Cheeseman, J. R.; Scalmani, G.; Barone, V.; Mennucci, B.; Petersson, G. A.; Nakatsuji, H.; Caricato, M.; Li, X.; Hratchian, H. P.; Izmaylov, A. F.; Bloino, J.; Zheng, G.; Sonnenberg, J. L.; Hada, M.; Ehara, M.; Toyota, K.; Fukuda, R.; Hasegawa, J.; Ishida, M.; Nakajima, T.; Honda, Y.; Kitao, O.; Nakai, H.; Vreven, T.; Montgomery, J. A., Jr.; Peralta, J. E.; Ogliaro, F.; Bearpark, M.; Heyd, J. J.; Brothers, E.; Kudin, K. N.; Staroverov, V. N.; Kobayashi, R.; Normand, J.; Raghavachari, K.; Rendell, A.; Burant, J. C.; Iyengar, S. S.; Tomasi, J.; Cossi, M.; Rega, N.; Millam, J. M.; Klene, M.; Knox, J. E.; Cross, J. B.; Bakken, V.; Adamo, C.; Jaramillo, J.; Gomperts, R.; Stratmann, R. E.; Yazyev, O.; Austin, A. J.; Cammi, R.; Pomelli, C.; Ochterski, J. W.; Martin, R. L.; Morokuma, K.; Zakrzewski, V. G.; Voth, G. A.; Salvador, P.; Dannenberg, J. J.; Dapprich, S.; Daniels, A. D.; Farkas; Foresman, J. B.; Ortiz, J. V.; Cioslowski, J.; Fox, D. J.*Gaussian 09*, revision D.01; Gaussian, Inc.: Wallingford, CT, 2009.

(14) O'Boyle, N. M.; Banck, M.; James, C. A.; Morley, C.; Vandermeersch, T.; Hutchison, G. R. Open Babel: an open chemical toolbox. *J. Cheminform* **2011**, *3*, 33.

(15) Becke, A. D. Density-functional exchange-energy approximation with correct asymptotic behavior. *Phys. Rev. A: Gen. Phys.* **1988**, *38* (6), 3098−3100.
(16) Becke, A. D. Density-functional thermochemistry. III. The role of exact exchange. *J. Chem. Phys.* **1993**, *98* (7), 5648−5652.
(17) Lee, C.; Yang, W.; Parr, R. G. Development of the Colle-Salvetti correlation-energy formula into a functional of the electron density. *Phys. Rev. B* **1988**, *37*, 785−789.
(18) Marenich, A. V.; Cramer, C. J.; Truhlar, D. G. Universal solvation model based on solute electron density and on a continuum model of the solvent defined by the bulk dielectric constant and atomic surface tensions. *J. Phys. Chem. B* **2009**, *113* (18), 6378−6396.
(19) Graafland, T.; Wagenaar, A.; Kirby, A. J.; Engberts, J. B. F. N. Structure and reactivity in intramolecular catalysis. Catalysis of sulfonamide hydrolysis by the neighboring carboxyl group. *J. Am. Chem. Soc.* **1979**, *101* (23), 6981−91.
(20) Kubrakova, I. V.; Formanovsky, A. A.; Mikhura, I. V. Facile hydrolytic cleavage of a sulfonamide bond under microwave irradiation. *Mendeleev Commun.* **1999**, *9*, 65−66.
(21) Lopes, F.; Moreira, R.; Iley, J. Acyloxymethyl as a drug protecting group. Part 5. Kinetics and mechanism of the hydrolysis of tertiary N-acyloxymethylsulfonamides. *J. Chem. Soc., Perkin Trans. 2* **1999**, *3*, 431−439.
(22) Bialk-Bielinska, A.; Stolte, S.; Matzke, M.; Fabianska, A.; Maszkowska, J.; Kolodziejska, M.; Liberek, B.; Stepnowski, P.; Kumirska, J. Hydrolysis of sulphonamides in aqueous solutions. *J. Hazard. Mater.* **2012**, *221*−*222*, 264−274.
(23) Wood, J. M.; Hinchliffe, P. S.; Davis, A. M.; Austin, R. P.; Page, M. I. Hydrolysis of a sulfonamide by a novel elimination mechanism generated by carbanion formation in the leaving group. *Chem. Commun. (Cambridge, U. K.)* **2002**, *7*, 772−773.
(24) Ryabov, A. D.*Practical Kinetics and Mechanisms of Chemical and Enzymatic Reactions*; Cambridge Scholars Publishing, Lady Stephenson Library: Newcastle upon Tyne, U.K., 2021.
(25) Popescu, D.-L.; Chanda, A.; Stadler, M. J.; Mondal, S.; Tehranchi, J.; Ryabov, A. D.; Collins, T. J. Mechanistically inspired design of FeIII-TAML peroxide-activating catalysts. *J. Am. Chem. Soc.* **2008**, *130* (37), 12260−12261.
(26) Somasundar, Y.; Shen, L. Q.; Hoane, A. G.; Kaaret, E. Z.; Warner, G. R.; Ryabov, A. D.; Collins, T. J. Predicting properties of iron(III) TAML activators of peroxides from their III/IV and IV/V reduction potentials or a lost battle to peroxidase. *Chem. - Eur. J.* **2020**, *26* (64), 14738−14744.
(27) Ferroni, G.; Antonetti, G.; Romanetti, R.; Galea, J. Potentiometric study of the dissociation and association equilibriums of dihydrogen phosphate ion, in 3M potassium chloride ions between 5 and 65.deg. *Bull. Soc. Chim. Fr.* **1973**, *12*, 3269−3273.
(28) Ferroni, G. Potentiometric studies on association and dissociation equilibriums of orthophosphoric acid, in water-potassium chloride 3M medium, at 25°. *Electrochim. Acta* **1976**, *21* (4), 283−6.
(29) O'Conner, C. J.; Wallace, R. G. A phosphate-catalyzed acyl transfer reaction. Hydrolysis of 4-nitrophenyl acetate in phosphate buffers. *Aust. J. Chem.* **1984**, *37* (12), 2559−69.
(30) Adams, W. A.; Preston, C. M.; Chew, H. A. M. A high-pressure conductivity and laser Raman spectroscopic study of aqueous orthophosphate solutions at 25°C. *J. Chem. Phys.* **1979**, *70* (5), 2074−80.
(31) Mata, I.; Alkorta, I.; Molins, E.; Espinosa, E. Electrostatics at the origin of the stability of phosphate-phosphate complexes locked by hydrogen bonds. *ChemPhysChem* **2012**, *13* (6), 1421−1424.

https://doi.org/10.1021/acs.inorgchem.2c03854
Inorg. Chem. 2023, 62, 639−647